3-D elastic wave scattering by a layer containing vertical periodic fractures

Seiji Nakagawa [a], Kurt T. Nihei, Larry R. Myer, and Ernest L. Majer

Earth Sciences Division, Lawrence Berkeley National Laboratory, Berkeley, California

Received:

Running title: 3-D elastic wave scattering by fractures

Abbreviated title: 3-D Elastic wave scattering by a layer containing vertical periodic fractures

[a]Electronic-mail: snakagawa@lbl.gov

ABSTRACT

Elastic wave scattering off a layer containing a single set of vertical periodic fractures is examined using a numerical technique based on the work of Hennion et al. [*J. Acoust. Soc. Am.*, **87(5)**, 1861-1870 (1990)] This technique combines the finite element method and plane wave method to simulate three-dimensional scattering off a two-dimensional fractured layer structure. Each fracture is modeled explicitly, so that the model can simulate both discrete arrivals of scattered waves from individual fractures and multiply scattered waves between the fractures. Using this technique, we examine changes in scattering characteristics of plane elastic waves as a function of wave frequency, angle of incidence, and fracture properties such as fracture stiffness, height, and regular and irregular spacing.

PACS numbers: 43.20.Gp, 43.20.Px, 43.58.Ta

I. INTRODUCTION

Fractures in sedimentary rock can have a significant impact on the production of gas and liquids in the subsurface. These fractures often are near regularly spaced and near vertical with a preferred orientation in the horizontal plane due to regional geological stresses (Figure 1). The conventional approach for characterizing these fractures using seismic (elastic) waves treats a fractured rock as an equivalent, homogeneous transversely isotropic medium with the elastic symmetry axis aligned in the fracture-normal direction. This methodology has been adopted by many researchers to examine the seismic properties of fractured rock in physical experiments, [1] theoretical modeling, [2,3] numerical studies using the finite difference method [4] and interpretation of field data. [5] A particularly important result from such research is that a geological unit containing aligned fractures can exhibit azimuthal anisotropy (around a vertical axis) in the velocity and amplitude of scattered elastic waves, which can be used for fracture detection and characterization. This effective medium approach, however, neglects frequency-dependent wave phenomena such as scattering off and wave channeling along discrete fractures, which become increasingly important to consider in high-resolution seismic surveys using higher-frequency waves with wavelengths comparable to the fracture spacing.

Understanding these frequency-dependent effects of fractures on seismic behavior is critical for designing field measurements and collecting data. For the surveys to cover fractures of many scales, a broad range of frequency needs to be employed. Conversely, if fractures of certain size range are to be detected and characterized, a proper frequency range that should be used in the survey needs to be known. These measurements can be performed at many scales, ranging from the well-logging (kilohertz), single-well (hundreds of hertz to kilohertz), cross-well (hundreds of

hertz) to the VSP (vertical seismic profiling) and surface seismic (10 to 100 hertz) scales. The data should be collected using multi-component sensors to capture the effect of fracture anisotropy augmented by wave frequency and fracture scale. These data can help to map and characterize fractures at many scales if the frequency-dependent and anisotropic effect of fracture properties on seismic waves is understood. To this end, numerical studies have been performed to examine high-frequency, three-dimensional seismic (elastic) wave scattering by fractures with a range of geometric and material properties.

The scattering of elastic waves off individual fractures can be simulated explicitly using a variety of numerical techniques. For high-frequency wave scattering problems, the boundary element method (BEM) has been used for its accuracy in modeling the stress singularity and wave diffractions generated at the ends of fractures. [6-8] Typically, the BEM computation is performed by modeling a fracture as internal boundaries, and a series of linear systems of equations is solved for unknown crack- (fracture-) opening displacements at each frequency (frequency-domain BEM) or time step (time-domain BEM). Alternatively, for large-scale problems with heterogeneous distribution of material properties in the background medium of fractures, explicit, time-domain finite difference methods (FDM) have been used. This is achieved by modeling individual fractures as thin compliant, orthotropic zones with a thickness equal to a single finite difference cell. [9] Using this method, Schoenberg et al. [10] studied two-dimensional elastic wave scattering off an elastic layer containing a large number of aligned vertical fractures. These simulations showed that an incident compressional wave can generate significantly large scattered shear waves when the fracture spacing is on the order of the shear wave wavelength.

However, the direct extension of the existing numerical methods such as the BEM and FDM to three-dimensional fractured systems, which is necessary for studying the azimuthal anisotropy of scattered waves, is still difficult and not commonly performed. This is primarily because the BEM requires a large computing time to solve multiple, linear system of equations with a large, densely populated system matrix while the size of available computer memory limits the size of problems solvable using the FDM.

In this paper, we show that if the aligned fractures in a single horizontal layer are periodic and extend infinitely in one of the horizontal directions, the three-dimensional scattering of elastic waves off these fractures can be examined by using an efficient numerical technique that involves only a two-dimensional finite element mesh. The method is based on the numerical technique developed by Hennion et al. [11] and Hlakdy-Hennion and Decarpigny [12] for acoustic (pressure) wave scattering by heterogeneous, periodic, and elastic structures. By extending this technique to incident elastic waves, we compute frequency domain responses and subsequently time domain seismograms of plane elastic waves scattered from the periodic, two-dimensional fractured structure for arbitrary angles of incidence.

II. THEORY

A. 3D wave scattering by a 2D periodic structure

In this paper, we examine the scattering of incident plane waves by an array of vertical fractures that extends infinitely in a single horizontal direction within an elastic layer (Figure 2). The fractured layer is divided into an array of periodic cells in the x, z plane, with a thickness L_z and a width L_x. The Cartesian coordinate system used throughout this paper is defined in the figure with the z direction pointing downward parallel to the fractures and the x direction parallel

to the fracture-normal direction. The geometry of such a model is characterized by the continuous translational symmetry in the *y* direction, and the discrete translational symmetry with a period L_x in the *x* direction. The homogeneous halfspaces above and below the fractured layer are denoted Ω_- and Ω_+, respectively. A single unit cell within the fractured layer, which can be heterogeneous, is denoted Ω_0, and the surrounding boundaries are defined as $\Gamma_{z+} \equiv \Omega_+ \cap \Omega_0$ and $\Gamma_{z-} \equiv \Omega_- \cap \Omega_0$, and the periodic boundaries on the sides are $\Gamma_{x-} \equiv \Omega_0$ (x=0) and $\Gamma_{x+} \equiv \Omega_0$ (x=L_x). The numerical technique shown in the following subsections models the homogeneous domains Ω_- and Ω_+ using plane wave theory, and the fractured domain Ω_0 using the finite element method (FEM).

B. Elastic plane wave propagation in a homogeneous domain

In an isotropic and homogeneous elastic medium with P (compressional) and S (shear) wave velocities C_P and C_S, respectively, and material density ρ, the particle displacement of monochromatic plane waves with a frequency ω propagating in the down-going (positive-*z*) direction is given by

$$\begin{aligned}
\mathbf{u}^+ &= \begin{bmatrix} u_x \\ u_y \\ u_z \end{bmatrix} = \left[\hat{\mathbf{v}}_{Sv} a_{Sv}^+ e^{ik_z^S z} + \hat{\mathbf{v}}_{Sh} a_{Sh}^+ e^{ik_z^S z} + \hat{\mathbf{v}}_P a_P^+ e^{ik_z^P z} \right] e^{i\left(k_x x + k_y y - \omega t\right)} \\
&= \begin{bmatrix} k_x/k & -k_y/k & 0 \\ k_y/k & k_x/k & 0 \\ 0 & 0 & 1 \end{bmatrix} \begin{bmatrix} -k_z^S/k_S & 0 & k/k_P \\ 0 & 1 & 0 \\ k/k_S & 0 & k_z^P/k_P \end{bmatrix} \begin{bmatrix} e^{ik_z^S z} & 0 & 0 \\ 0 & e^{ik_z^S z} & 0 \\ 0 & 0 & e^{ik_z^P z} \end{bmatrix} \begin{bmatrix} a_{Sv}^+ \\ a_{Sh}^+ \\ a_P^+ \end{bmatrix} e^{i\left(k_x x + k_y y - \omega t\right)}, \quad (1) \\
&\equiv \mathbf{R}^T \mathbf{U}^+ \mathbf{E}^+(z) \mathbf{a}^+ e^{i\left(k_x x + k_y y - \omega t\right)}
\end{aligned}$$

where $k_z^P = \sqrt{k_P^2 - k^2}$ and $k_z^S = \sqrt{k_S^2 - k^2}$ are the vertical components of P- and S-wave wavenumber vectors with amplitudes k_P and k_S, respectively, k is the horizontal wavenumber

given by $k = \sqrt{k_x^{\,2} + k_y^{\,2}}$ where k_x and k_y are the *x*- and *y*-direction wavenumbers each of which is preserved when the wave is scattered by a horizontal boundary. "*i*" in the exponent is $\sqrt{-1}$. **R** is the rotation matrix around the *z* axis, and the superscript ^{T} indicates the matrix transposition. **R** rotates the unit particle motion vectors $\hat{\mathbf{v}}_{Sv}$, $\hat{\mathbf{v}}_{Sh}$, and $\hat{\mathbf{v}}_P$ for the three independent wave modes to each column vector in the matrix $\mathbf{U}^+$. Components a_{Sv}^+, a_{Sh}^+, and a_P^+ of the column vector $\mathbf{a}^+$ corresponding to these vectors give the amplitude of individual wave modes, and each mode type is denoted in the subscript, i.e., *P* for the P wave, *Sh* for the horizontally polarized S wave, and *Sv* for the remaining component of the S wave. Superscripts "+" indicate down-going waves. Three stress components on a horizontal plane are computed by

$$\boldsymbol{\sigma}^+ = \begin{bmatrix} \sigma_{xz} \\ \sigma_{yz} \\ \sigma_{zz} \end{bmatrix} = \mathbf{R}^T \mathbf{S}^+ \mathbf{E}^+(z) \mathbf{a}^+ e^{i(k_x x + k_y y - \omega t)}, \tag{2}$$

where the matrix $\mathbf{S}^+$ is obtained by applying the elastic Hooke's law to Eq.(1),

$$\mathbf{S}^+ \equiv i\omega\rho \begin{bmatrix} -\left[1 - 2(k/k_S)^2\right] & 0 & 2kk_z^P/(k_S k_P) \\ 0 & k_z^S/k_S & 0 \\ 2kk_z^S/k_S^2 & 0 & \left[1 - 2(k/k_S)^2\right] \cdot k_S/k_P \end{bmatrix}. \tag{3}$$

For plane waves propagating in the up-going (negative *z*) direction, the displacement and stress are obtained by changing the signs of k_z^P and k_z^S in Eqs.(1) through (3).

C. Finite element method for the fractured domain

For the domain containing fractures, the FEM is used to model the displacement and stress fields that can be highly complex due to the scattering of waves. The variational equation of

three-dimensional, elastodynamic problems for monochromatic wave propagation can be written as [13]

$$\int_V w_{i,j} C_{ijkl} u_{k,l} dV - \omega^2 \int_V w_i \rho \delta_{ij} u_j dV - \int_V w_i b_i dV - \int_S w_i t_i dS = 0 \quad (i, j, k, l = x, y, z), \qquad (4)$$

where u_j and w_i are the displacement and virtual displacement, b_i and t_i are the body force and surface traction, δ_{ij} is the Kronecker delta and C_{ijkl} is the fourth-rank tensor of elastic moduli. The summation rule applies to the repeated indices in the above equation and the rest of the equations in this subsection. The domain of integration in space and the domain boundary are denoted V and S, respectively. It is noted that the volumetric integrals in the first and the second terms represent the virtual strain energy and kinetic energy, respectively, and the third and fourth terms are the external virtual work done by the body force and the surface traction.

Because of the continuous translational geometric symmetry in the y direction and of the monochromatic plane incident waves, terms dependent on the parameters y and ω are both factored out of the displacement and force variables u_j, w_i, b_i and t_i. For example, u_j and w_i can be expressed as

$$u_j(x, y, z, t) = u_j(x, z) e^{i(k_y y - \omega t)} \qquad (5)$$

$$w_i(x, y, z, t) = w_i(x, z) e^{i(k_y y - \omega t)}. \qquad (6)$$

"i"($=\sqrt{-1}$) in the exponent should not be confused with the indeces "i"($=x, y, z$) in the subscript. We introduce the following variables for later use:

$$\tilde{u}_{k,l} = \begin{cases} u_{k,l}(x, z) & l = x, z \\ ik_y \cdot u_k(x, z) & l = y \end{cases}, \qquad (7)$$

$$\tilde{w}_{i,j} = \begin{cases} w_{i,j}(x,z) & j = x,z \\ ik_y \cdot w_i(x,z) & j = y \end{cases}, \quad (8)$$

where $ik_y = \sqrt{-1}\,k_y$. When these expressions are introduced into Eq.(4), by denoting the two-dimensional domain Ω and boundary Γ corresponding to the three-dimensional domain V and boundary S,

$$e^{-i\omega t}\int e^{+2ik_y y}dy \cdot \left[\int_\Omega \tilde{w}_{i,j}C_{ijkl}\tilde{u}_{k,l}d\Omega - \omega^2\int_\Omega w_i\rho\delta_{ij}u_j d\Omega - \int_\Omega w_i b_i d\Omega - \int_\Gamma w_i t_i d\Gamma\right] = 0. \quad (9)$$

Because of the periodicity, the integration in the y direction can be taken for a single period, i.e., $[0, 2\pi/k_y]$. The time- and y-coordinate-dependent terms can be dropped off the equation, and the variational equation becomes

$$\int_\Omega w_{ij}C_{ijkl}u_{kl}d\Omega - \omega^2\int_\Omega w_i\rho\delta_{ij}u_j d\Omega = \int_\Omega w_i b_i d\Omega + \int_\Gamma w_i t_i d\Gamma. \quad (10)$$

We model fractures explicitly as internal boundaries with surface traction. The stress singularity arising at the ends of the fractures is treated by using the distorted mesh (quarter-node mesh) technique. [14,15] The work term for the boundaries (the second term on the right-hand side of the equation) can be divided into three parts, one for the external boundary Γ_{ext} and the other two for the fracture surfaces Γ_{f+} and Γ_{f-}.

$$\int_\Gamma w_i t_i d\Gamma = \int_{\Gamma_{ext}} w_i t_i d\Gamma + \int_{\Gamma_{f+}} w_i^+\sigma_{ij}^+ n_j^+ d\Gamma + \int_{\Gamma_{f-}} w_i^-\sigma_{ij}^- n_j^- d\Gamma. \quad (11)$$

The two opposing surfaces of the fracture are labeled with subscripts "+" and "-" and have unit normal vectors n_j^+ and n_j^-, respectively. Using these vectors, we wrote the tractions in terms of the stress components σ_{ij}^+ and σ_{ij}^-. The superscripts on the variables are to emphasize the surface of the fracture on which the variables are defined. Because we assume mathematical fractures

that have no thickness, the geometry of the two surfaces is identical, which results in $\Gamma_{f+} = \Gamma_{f-} \equiv \Gamma_f$ and $n_j^- = -n_j^+$. Therefore,

$$\int_{\Gamma} w_i t_i d\Gamma = \int_{\Gamma_{ext}} w_i t_i d\Gamma + \int_{\Gamma_f} w_i^+ \sigma_{ij}^+ (-n_j^-) d\Gamma + \int_{\Gamma_f} w_i^- \sigma_{ij}^+ n_j^- d\Gamma . \quad (12)$$

For small displacement and stress introduced by wave propagation, boundary conditions on the fracture (the linear slip or displacement-discontinuity boundary conditions) can be stated as

$$\sigma_{ij}^+ = \sigma_{ij}^- \equiv \sigma_{ij} , \quad (13)$$

$$\sigma_{ij} n_j^- = t_i^- = \kappa_{ij} (u_j^+ - u_j^-) , \quad (14)$$

where κ_{ij} is the fracture stiffness tensor. [16,17] Using these relationships, the Eq.(12) becomes

$$\int_{\Gamma} w_i t_i d\Gamma = \int_{\Gamma_{ext}} w_i t_i d\Gamma - \int_{\Gamma_f} (w_i^+ - w_i^-) \kappa_{ij} (u_i^+ - u_i^-) d\Gamma . \quad (15)$$

The second term on the right-hand side of the equation can now be seen as the internal virtual work (strain energy) stored in the fracture. By introducing Eq.(15) into Eq.(10), the variational equation becomes

$$\begin{aligned} &\int_{\Omega} w_{ij} C_{ijkl} u_{kl} d\Omega + \int_{\Gamma_f} (w_i^+ - w_i^-) \kappa_{ij} (u_i^+ - u_i^-) d\Gamma - \omega^2 \int_{\Omega} w_i \rho \delta_{ij} u_j d\Omega \\ &- \int_{\Omega} w_i b_i d\Omega - \int_{\Gamma_{ext}} w_i t_i d\Gamma = 0 \end{aligned} . \quad (16)$$

This equation is discretized using a nodal displacement vector **U** and a virtual nodal displacement vector **W**. [13] In vector notation, the discrete form of the equation is

$$\mathbf{W}^T (\mathbf{K}_b \mathbf{U} + \mathbf{K}_f \mathbf{U} - \omega^2 \mathbf{M} \mathbf{U} - \mathbf{F}) = 0 , \quad (17)$$

where $\mathbf{K}_b$, $\mathbf{K}_f$, and $\mathbf{M}$ are the FEM bulk stiffness, fracture stiffness and mass matrices, respectively, and $\mathbf{F}$ is the FEM load vector, corresponding to each domain and boundary integral in the variational equation. Because $\mathbf{W}^T$ is for arbitrary virtual displacement, it can be dropped and

$$\mathbf{KU} \equiv (\mathbf{K}_b + \mathbf{K}_f - \omega^2 \mathbf{M})\mathbf{U} = \mathbf{F}. \qquad (18)$$

This is the finite element equation that is solved for unknown nodal displacement. Because the system stiffness matrix $\mathbf{K}$ and the load vector $\mathbf{F}$ are computed from numerical integrations within and along the two-dimensional domain Ω, the FEM mesh required for this computation is two-dimensional although each node has three degrees of freedom in displacement (e.g., Figure 3).

D. Coupling between plane wave fields and FEM mesh

Hannion et al. [11] have given a detailed description of the method to couple plane acoustic wave fields and an FEM mesh. Here, we present their method for the elastic case.

Because of the discrete translational symmetry (periodicity) in the x direction and the plane incident waves, the scattered wavefield within the halfspaces Ω_- and Ω_+ can be expressed by a superposition of an infinite series of plane waves with discrete x-direction wavenumbers. In order to solve the problem numerically, this series is truncated at a finite number M. Therefore the wavenumber for the n^{th} mode is given by $k_{nx}=k_{0x}+2\pi(n/L_x)$ ($n=-M, -M+1, \ldots, 0, \ldots, +M$) where k_{x0} is the x-direction wavenumber for an incident plane wave, which we previously denoted k_x. In this study, the series truncation number M was determined so that the total number of the modes $2M+1$ is equal to the number of FEM nodes along the boundaries Γ_{z+} and Γ_{z-}.

We first examine the plane wave field in the domain Ω_+ along the boundary Γ_{z+}. Since only down-going waves exist in this domain, the displacement and stress are

$$\mathbf{u}^+ = \sum_{n=-M}^{+M} \mathbf{R}_n^T \mathbf{U}_n^+ \mathbf{a}_n^+ e^{ik_{nx}x}, \tag{19}$$

$$\boldsymbol{\sigma}^+ = \sum_{n=-M}^{+M} \mathbf{R}_n^T \mathbf{S}_n^+ \mathbf{a}_n^+ e^{ik_{nx}x}, \tag{20}$$

where $\mathbf{R}_n^T$, $\mathbf{U}_n^+$, $\mathbf{S}_n^+$, and $\mathbf{a}_n^+$ are obtained by substituting k, k_z^P, and k_z^S in Eqs.(1) through (3) by wavenumbers k_{nx}, k_{nz}^P, and k_{nz}^S of corresponding modes. The dependency on the term $e^{i(k_y y-\omega t)}$ is understood and dropped from Eqs.(19), (20), and the following derivations. Also, without losing generality, the origin of the z coordinate is defined on Γ_{z+}, which has eliminated $\mathbf{E}^+(z=0)=\mathbf{E}$ (identity matrix) from the equations.

Within the FEM domain Ω_0 along Γ_{z+}, a similar decomposition of the displacement field can be obtained from a truncated Fourier series,

$$\mathbf{u}^+ = \sum_{n=-M}^{+M} \mathbf{c}_n^+ e^{ik_{nx}x}, \tag{21}$$

where the coefficient vectors $\mathbf{c}_n^+$ can be computed from the displacement along Γ_{z+} by

$$\mathbf{c}_n^+ = \frac{1}{L_x}\int_{-L_x/2}^{+L_x/2} \mathbf{u}^+(x) e^{-ik_{nx}x} dx. \tag{22}$$

From term-by-term comparison between Eqs.(19) and (21), coefficient vectors $\mathbf{a}_n^+$ can be expressed via $\mathbf{c}_n^+$ as $\mathbf{a}_n^+ = \left(\mathbf{U}_n^+\right)^{-1} \mathbf{R}_n \mathbf{c}_n^+$. By introducing this relationship into Eq.(20), the stress (or traction) along the boundary can be computed by

$$\boldsymbol{\sigma}^+ = \sum_{n=-M}^{+M} \mathbf{R}_n^T \mathbf{S}_n^+ \left(\mathbf{U}_n^+\right)^{-1} \mathbf{R}_n \mathbf{c}_n^+ e^{ik_{nx}x}. \tag{23}$$

This relationship is important because it explicitly gives the traction along the boundary via displacement, hence eliminating the necessity for the unknown parameters of the plane wave field within Ω_+.

We now write Eq. (23) via nodal displacement. The boundary displacement and traction (or stress) can be expressed by their nodal values as

$$\mathbf{u}_e^+(x) = \sum_{I=1}^{N_{nx}} N_{eI}(x)\mathbf{u}^{+eI}, \tag{24}$$

$$\mathbf{t}_e^+(x)\left(=\boldsymbol{\sigma}^+\right) = \sum_{I=1}^{N_{nx}} N_{eI}(x)\boldsymbol{\sigma}^{+eI}, \tag{25}$$

where the summation is performed only for the boundary nodes along a single element e, and $N_{eI}(x)$ are the shape functions for nodes I (I=1, 2, …, N_{nx}). $\boldsymbol{u}^{+eI}$ and $\boldsymbol{\sigma}^{+eI}$ are the nodal displacement and stress. The displacement along the boundary is given by a union of the displacement for each element as

$$\mathbf{u}^+(x) = \bigcup_{e=1}^{N_{ex}} \mathbf{u}_e^+(x), \tag{26}$$

where N_{ex} is the number of elements along Γ_{z+}. Therefore the coefficient vectors $\mathbf{c}_n^+$ in Eq. (23) are computed from Eqs. (22) and (26) as

$$\begin{aligned}\mathbf{c}_n^+ &= \frac{1}{L_x}\sum_{e=1}^{N_{ex}} e^{-ik_{nx}x_e}\int_{-h_e/2}^{h_e/2}\mathbf{u}_e^+(x')e^{-ik_{nx}x'}dx' \\ &= \frac{1}{L_x}\sum_{e=1}^{N_{ex}} e^{-ik_{nx}x_e}\sum_{I=1}^{N_{nx}}\int_{-h_e/2}^{h_e/2} N_{eI}(x')e^{-ik_{nx}x'}dx'\mathbf{u}^{+eI}, \\ &\equiv \mathbf{A}_n^+\mathbf{U}^+\end{aligned} \tag{27}$$

where h_e is the width of each element e (e=1, 2, …, N_{ex}), x_e is the x coordinate of the element center, and $\mathbf{U}^+$ is a column vector containing the nodal displacement vectors along the boundary.

x' indicates the local coordinate defined around x_e ($-h_e/2 \le x' \le h_e/2$). For the special case when the width of the elements along the boundary is constant ($\equiv h$) and $N_{nx}=3$, the matrix $\mathbf{A}_n^+$ becomes

$$\mathbf{A}_n^+ = \left[\theta_{n11}^+ \mathbf{E} \quad \theta_{n12}^+ \mathbf{E} \quad (\theta_{n13}^+ + \theta_{n21}^+)\mathbf{E} \quad \theta_{n22}^+ \mathbf{E} \quad (\theta_{n23}^+ + \theta_{n31}^+)\mathbf{E} \quad \cdots \quad \theta_{nN_{ex}3}^+ \mathbf{E} \right], \quad (28)$$

where $\mathbf{E}$ is the 3x3 identity matrix and

$$\theta_{neI}^+ \equiv \frac{h \cdot e^{-ik_{nx}x_e}}{L_x} \int_{-h/2}^{+h/2} N_I(x') e^{-ik_{nx}x'} dx'. \quad (29)$$

The nodal forces on an element e along the boundary Γ_{z+} are computed by

$$\mathbf{f}_{eI}^+ = \int_{-h_e/2}^{h_e/2} N_{eI}(x') \mathbf{t}_e^+(x') dx', \quad (30)$$

where $\mathbf{t}_e^+ (= \boldsymbol{\sigma}^+)$ is the boundary traction computed using the plane wave solutions. From Eqs.(23) and (27), these forces can be computed from the nodal displacements on the boundary as

$$\mathbf{f}_{eI}^+ = e^{ik_{nx}x_e} \sum_{n=-M}^{M} \int_{-h_e/2}^{h_e/2} N_{eI}(x') e^{ik_{nx}x'} dx' \cdot \mathbf{R}_n^T \mathbf{S}_n^+ \left(\mathbf{U}_n^+ \right)^{-1} \mathbf{R}_n \mathbf{A}_n^+ \mathbf{U}^+. \quad (31)$$

Therefore, the load vector containing nodal force vectors along the boundary is given as a linear function of the nodal displacement. Again, when $h_e=h$ and $N_{nx}=3$, this is

$$\begin{aligned} \mathbf{F}^+ &= \left[\mathbf{f}_{11}^{+T} \quad \mathbf{f}_{12}^{+T} \quad (\mathbf{f}_{13}^{+T} + \mathbf{f}_{21}^{+T}) \quad \mathbf{f}_{22}^{+T} \quad (\mathbf{f}_{23}^{+T} + \mathbf{f}_{31}^{+T}) \quad \cdots \quad \mathbf{f}_{N_{ex}3}^{+T} \right]^T \\ &= L_x \sum_{n=-M}^{+M} (\mathbf{A}_n^+)^* \mathbf{R}_n^T \mathbf{S}_n^+ \left(\mathbf{U}_n^+ \right)^{-1} \mathbf{R}_n \mathbf{A}_n^+ \mathbf{U}^+ \equiv \Delta^+ \mathbf{U}^+ \end{aligned}, \quad (32)$$

where the superscript "*" indicates transposition and complex-conjugation of the matrix.

We now discuss the boundary Γ_{z-} for which the effect of the incident wave needs to be considered. Equations corresponding to Eqs. (19) and (20) for the displacement and stress are

$$\mathbf{u}^- = \sum_{n=-M}^{+M} \mathbf{R}_n^T \mathbf{U}_n^- \mathbf{a}_n^- e^{ik_{nx}x} + \mathbf{R}_0^T \mathbf{U}_0^+ \mathbf{a}_{Inc} e^{ik_{0x}x}, \tag{33}$$

$$\boldsymbol{\sigma}^- = \sum_{n=-M}^{+M} \mathbf{R}_n^T \mathbf{S}_n^- \mathbf{a}_n^- e^{ik_{nx}x} + \mathbf{R}_0^T \mathbf{S}_0^+ \mathbf{a}_{Inc} e^{ik_{0x}x}, \tag{34}$$

respectively, where $\mathbf{a}_{Inc}$ is a column vector containing the complex amplitude of an incident plane wave. Again, $\mathbf{E}^-$ was dropped from Eqs. (33) and (34) by defining the origin of the z axis on the boundary Γ_{z-}. From the Fourier expansion of the displacement as in Eq. (21), Eq. (33) yields the relationships

$$\mathbf{c}_n^- = \mathbf{R}_n^T \mathbf{U}_n^- \mathbf{a}_n^-, \; n \neq 0, \tag{35}$$

$$\mathbf{c}_0^- = \mathbf{R}_0^T \left(\mathbf{U}_0^- \mathbf{a}_0^- + \mathbf{U}_0^+ \mathbf{a}_{Inc} \right), \tag{36}$$

where $\mathbf{a}_n^-$ is the amplitude vector for the n^{th} reflected wave. $\mathbf{U}_n^-$ and $\mathbf{S}_n^-$ are obtained by changing the signs of the z-direction wavenumbers, i.e., $+k_{nz}^P \rightarrow -k_{nz}^P$ and $+k_{nz}^S \rightarrow -k_{nz}^S$, in the definitions for $\mathbf{U}_n^+$ and $\mathbf{S}_n^+$. By eliminating the unknown reflected plane wave amplitudes $\mathbf{a}_n^-$ using Eqs.(35) and (36), Eq.(34) becomes

$$\boldsymbol{\sigma}^- = \sum_{n=-M}^{+M} \mathbf{R}_n^T \mathbf{S}_n^- \left(\mathbf{U}_n^- \right)^{-1} \mathbf{R}_n \mathbf{A}_n^- \mathbf{U}_b^- e^{ik_{nx}x} + \mathbf{R}_0^T \left[\mathbf{S}_0^+ - \mathbf{S}_0^- \left(\mathbf{U}_0^- \right)^{-1} \mathbf{U}_0^+ \right] \mathbf{a}_{Inc} e^{ik_{0x}x}, \tag{37}$$

where $\mathbf{A}_n^-$ is also defined by changing the signs of wavenumbers in $\mathbf{A}_n^+$. Finally, the load vector can be obtained through the same procedure as for $\mathbf{F}^+$ but with $\mathbf{t}_e^- = -\boldsymbol{\sigma}^-$, yielding

$$\mathbf{F}^- = \Delta^- \mathbf{U}^- + \overline{\mathbf{F}}, \tag{38}$$

where $\overline{\mathbf{F}}$ is the known term (incident wave term) arising from the second term in the right-hand side of Eq.(37). Terms containing unknown nodal displacement vectors $\mathbf{U}^+$ and $\mathbf{U}^-$ in Eqs.(32) and (38) are absorbed into the stiffness matrix of the FEM equation (18) during the assembly of the matrix.

E. Periodic boundary and matrix condensation

Along the boundaries Γ_{x-} and Γ_{x+}, dynamic periodic boundary conditions are applied by using the Floquet-Bloch theory. If the finite element matrix equation (18) is rearranged as

$$\begin{bmatrix} \mathbf{K}_{11} & \mathbf{K}_{12} & \mathbf{K}_{13} \\ \mathbf{K}_{21} & \mathbf{K}_{22} & \mathbf{K}_{23} \\ \mathbf{K}_{31} & \mathbf{K}_{32} & \mathbf{K}_{33} \end{bmatrix} \begin{bmatrix} \mathbf{U}_1 \\ \mathbf{U}_2 \\ \mathbf{U}_3 \end{bmatrix} = \begin{bmatrix} \overline{\mathbf{F}}_1 \\ \mathbf{F}_2 \\ \mathbf{F}_3 \end{bmatrix} \tag{39}$$

where subscript "$_1$" denotes non-periodic displacement and force vectors, and "$_2$" and "$_3$" indicate periodic displacement and load vectors on boundaries Γ_{x-} and Γ_{x+}, respectively. Submatrices relating these vectors are given by $\mathbf{K}_{ij}$ (i, j=1, 2, 3). The "bar" on the load vector $\mathbf{F}_1$ indicates that this is a known term. It is noted that this equation is underdetermined, and additional constraints (boundary conditions) need to be applied. The dynamic periodic boundary condition leads to the following relationships between nodal displacement and traction on the boundaries Γ_{x-} and Γ_{x+} as

$$\mathbf{U}_3 = \mathbf{U}_2 e^{+ik_{0x}L_x}, \tag{40}$$

$$\mathbf{F}_2 = -\mathbf{F}_3 e^{-ik_{0x}L_x}. \tag{41}$$

Using these relationships, the matrix equation (39) can be condensed as

$$\begin{bmatrix} \mathbf{K}_{11} & \mathbf{K}_{12} + \mathbf{K}_{13} e^{+ik_{0x}L_x} \\ \mathbf{K}_{21} + \mathbf{K}_{31} e^{-ik_{0x}L_x} & \mathbf{K}_{22} + \mathbf{K}_{23} e^{+ik_{0x}L_x} + \mathbf{K}_{32} e^{-ik_{0x}L_x} + \mathbf{K}_{33} \end{bmatrix} \begin{bmatrix} \mathbf{U}_1 \\ \mathbf{U}_2 \end{bmatrix} = \begin{bmatrix} \overline{\mathbf{F}}_1 \\ \mathbf{0} \end{bmatrix}. \tag{42}$$

This is the FEM equation that is solved to obtain complex displacements on the FE mesh for a given combination of an incident wave frequency ω and horizontal wavenumbers k_x and k_y. From the displacement along the boundaries Γ_{x-} and Γ_{x+}, $\mathbf{c}_n^-$ and $\mathbf{c}_n^+$ can be computed using relationships such as in Eq. (27), and subsequently, the plane wave amplitude coefficients $\mathbf{a}_n^-$ and $\mathbf{a}_n^+$ are obtained (e.g., from Eqs. (35) and (36)). Finally, the displacement and stress fields for domains Ω_- and Ω_+ are computed by superposition of plane waves with a range of discrete horizontal wave numbers (Eqs.(19), (20), (33), and (34)).

Using this hybrid technique, the elastic wavefield within and outside the layer containing periodically spaced fractures can be computed for an incident plane wave. Figure 4 shows snapshots of a compressional wave propagating across a periodically fractured layer as cubes cut out of three-dimensional wavefields. Only the vertical (z) component of displacement is shown. In this particular model, the fracture spacing h is 4 m, the height H is 8m, and the stiffness is zero, i.e., completely open fractures. Except for the fractures, the entire field is isotropic and homogeneous with P- and S-wave velocities of 3000 m/sec and 1731 m/sec, respectively, and the material density of 2100 kg/m^3. The incident plane P wave has an azimuthal angle of 45° (measured from the x axis around the vertical z axis) and a dip angle of 60° (measured from the horizontal plane), and is a Ricker wavelet of unit amplitude, with the central frequency of 444 Hz (the wavelength to fracture spacing ratio λ_P/h=1.69). The complex scattering behavior of the waves gives rise to the localized and trapped energy within the fractured layer as seen in Figure 4. The time-retarded radiation of this energy back to the upper halfspace manifests itself as the reverberation (coda) in measured reflection seismograms which we will discuss in detail in the following section.

III. EXAMPLES

A. Numerical model

For the remainder of this paper, we examine the scattering of an incident plane elastic wave by a single layer containing an array of plane-parallel, periodically spaced fractures using the hybrid numerical technique developed in the previous section. The analysis focuses on the reflection of an incident P wave by a fractured layer. Also, the background medium of the fractured layer is assumed to have the same properties as the surrounding homogeneous halfspaces (i.e., density 2100 kg/m^3 and P- and S-wave velocities 3000 m/sec and 1731 m/sec)

The hybrid plane wave-FEM method allows us to propagate a plane wave with arbitrary angles of incidence upon the fractured layer. By numerically simulating the scattering of plane waves propagating at a range of incidence angles, we can examine approximately the changes in the characteristics of reflected waves radiated far from a point source. In applications such as surface seismic surveys for oil and gas exploration, seismic sources and receivers are often located on a surface parallel or near-parallel to the fractured layer, and their relative distance and orientation are changed to probe fractures at different depths and orientations. To simulate this, we place a source and receiver pair on a single plane 100 m above the top of the fractured layer and change their locations symmetrically around a vertical axis on the plane. This results in changes in both azimuthal and dip angles (θ and ϕ) of incident waves (Figure 5).

To minimize numerical dispersion, the central frequency of Ricker wavelets used as incident pulses was chosen such that there were at least 10 nodes of FE mesh per S-wave wavelength. Although the FE meshes used for this study were rather coarse (for example, a mesh consisting

of 4x12 elements of 1 m x 1 m-size, 8-node quadrilateral serendipity elements with the mesh refinement near the fracture tips was used for equally spaced, 8 m-tall fractures as shown in Figure 3), the computed waveforms were in close agreement with the results obtained using finer meshes (e.g., 8x24-element model. We also checked the accuracy of the hybrid method using an accurate, two-dimensional frequency domain elastodynamic boundary element (BE) method. [7] In this exercise, the two methods were compared for waves propagating along the *x*, *z* plane. Because only a finite number of fractures was used in the BE model due to computational limitations, the BE results showed less coda than the results of the hybrid method that assumes an infinite series of fractures. However, early-time waveforms computed at locations near the fractures showed good agreement, indicating that the scattering of waves by individual fractures can be modeled accurately by the hybrid method.

The primary parameters used for the simulations are: 1) the central frequency of incident Ricker wavelet ("low" 111 Hz and "high" 332 Hz, corresponding to P-wave wavelengths of 27.1 m and 9.03 m), 2) fracture stiffness (for both normal and shear stiffnesses, "soft" 7.87×10^9 Pa/m and "stiff" 15.7×10^9 Pa/m, corresponding to normal incident P-wave transmission coefficients of 0.96 and 0.99 at 111 Hz, and 0.77 and 0.92 at 332 Hz), 3) fracture height ("short" 8 m and "tall" 16 m) and 4) irregularity of the fracture spacing (either regular 4 m intervals or irregular, alternating 3 m and 5 m intervals). Because there are still a large number of possible combinations among these parameters, only several illustrative examples of the results are presented in the following sections.

B. Waveforms as a function of incidence angles

For regularly spaced, "soft" 8 m-tall fractures, the waveforms of reflected waves for a unit-amplitude incident P wave were computed for a range of dip and azimuthal angles. The *z*, *t* (source-receiver azimuth direction) and *r* (source-receiver offset direction) components of the particle displacement, as defined in Figure 5, are shown in Figure 6a and 6b for both "low" and "high" frequency incident waves. The waveforms were computed at every 15° of increment in both dip and azimuthal angles. However, because the FEM system stiffness matrix becomes singular and the numerical code becomes unstable for the azimuthal angle of 90°, waveforms for 89.5° are shown instead. The direct waves were "muted" from the computed seismograms.

For the low-frequency case, the clear first arrivals in the *z*- and *r*-component seismograms are the reflected P waves that are followed by converted S waves. Using the notations in the theory, these S waves in the *z* and *r* components are the *Sv* waves, and S waves in the *t* component are the *Sh* waves. Reflections from the top and the bottom of the fractured layer are overlapping and difficult to distinguish from each other. With decreasing dip angle (measured from the horizontal plane) and increasing the source-receiver distance, amplitudes of the reflected waves increase significantly, making the detection of the fractured layer easier. An increase in the azimuthal angle (measured from the *x* axis) results in decreases in both *P*- and *S*-wave amplitudes. In particular, the amplitude of reflected *Sv* wave vanishes when the incident direction is parallel to the fractures. This can be explained by the source-receiver reciprocity: because no reflection of P waves (or S waves) occurs for an incident S wave with particle motion parallel to the fractures, when the source and the receiver are swapped, no reflection of S waves occur for an incident P

wave. The *Sh* component exhibits finite amplitudes at intermediate azimuthal angles because of the azimuthal anisotropy of the fractured layer, as shown by Schoenberg et al. [2]

For the high-frequency case, reflected waves show the same behavior as the low-frequency case. However, each arrival of the primary reflections is followed by coda that last for an extended period of time. Amplitudes of these coda compared to the leading, primary pulses are typically larger for smaller dip angles (i.e., larger incidence angles). We examine the behavior of coda more in detail in the following subsection.

C. Azimuthal variations of waveforms

From Figure 7a to 7e, azimuthal gathers of the *z*-component waveforms at a dip angle of 45° are shown for fractures with a range of properties. Within each plot, solid lines are computed using the hybrid technique, and the dotted lines are obtained by applying the static effective medium approximation to the fractured layer. In this approximation, the transversely isotropic elastic moduli of the layer containing fractures are computed by adding the compliance of the fractures to the matrix compliance. [18]

For the low-frequency case shown in Figure 7a, results of the hybrid method and the effective medium approximation are in excellent agreement. However, the development of coda results in significant differences in the waveforms for the high-frequency cases (Figure 7b). It is noted that the first-arriving part of the reflected P waves shows rather good agreement between the two methods. However, for small azimuthal angles, the distortion of the latter part of the first-arriving wavelet corresponding to the layer-bottom reflection results in an increase in mismatch

between the waveforms. The S-wave parts in the seismograms are difficult to identify because the amplitude of coda caused by the incident P wave is overwhelmingly large.

An increase in the fracture stiffness results in decreases in the amplitudes of reflected waves (Figure 7b and 7c). The relative effect is larger for the coda part of the wave, resulting in the first-arriving part of the P waves becoming easier to identify from the rest of the waveforms.

The simulations show that the relative amplitude of coda be reduced for the "taller" fractures as shown in Figure 7d (compare with Figure 7b). For this case, the P-wave reflection from the bottom of the layer is now clearly separated from the reflection from the top. Although the first-arriving parts of the individual reflections show good agreement with the static theory, the later-arriving parts of the wavelets shows significant discrepancies. The decrease in coda amplitude may result because longer fractures increase the forward scattering of an incident wave, [19] which reduces the contributions to the coda by waves scattered by distant fractures.

The periodic geometry and material properties of the fractures can be "perturbed" by modeling multiple fractures with a range of properties within a single periodic cell. Here we examine only the case for perturbed fracture spacing. In Figure 7e, waveforms are computed for periodic but irregular fracture intervals alternating between 3 m and 5 m in contrast to the regular 4 m intervals in Figure 7b. All other parameters are identical. Although the effect is not as strong as the "stiff" and "tall" fractures, the relative amplitude of the coda was, again, reduced compared to the reference case in Figure 7b. This decrease is due to the destructive interference between scattered waves due to the less ordered geometry of the fractures. It is interesting to note that the first-arriving part of the reflected P waves are well-approximated by the static effective medium

theory shown by the dotted lines even for small azimuthal angles. This was also observed for the "stiff" fracture case in Figure 7c.

D. Azimuthal variations of spectra

For the waveforms shown in the previous section, it is difficult to identify the azimuthal anisotropy due to the fractures using the complicated, seemingly random waveforms of the scattered high-frequency waves. To identify any consistent trends in the multiple scattering or resonance structures of the waveforms, we computed the amplitude spectra of the waveforms shown in Figure 7b to 7e excluding the direct waves. Each spectrum (Figure 8a to 8d) was normalized by the spectra of the incident wave. Spectra for waveforms computed using the static effective medium approximation are overlaid in dotted lines.

A comparison between the spectra computed by the hybrid plane wave-FEM method and the effective medium theory show that the results start to deviate at frequencies near 200 Hz corresponding to the fracture interval to P-wave wavelength ratio of $h/\lambda_P \sim 1/4$. In contrast, the sharp peaks in the spectra that contribute to the coda in the waveforms appear at frequencies above 300 Hz ($h/\lambda_P > 0.4$) for the regularly spaced fractures, and above 150 Hz ($h/\lambda_P > 0.2$) for the irregularly spaced fractures, indicating a strong correlation between the periodicity of the fracture interval and the coda frequency.

Also, for periodic fractures with regular spacings (Figure 8a, b, and c), the spectral profiles show a clear trend that shows upward shifts of the peaks (as indicated by solid triangles) with azimuthal angle. This trend becomes less obvious for irregular intervals (Figure 8d), but still noticeable changes as a function of azimuthal angle are present. The regularly spaced notches in the spectra are possibly caused by the tuning effect of the layer because they can be observed for

both hybrid and effective medium computations, and also, the intervals of notches are shorter (approximately half) for the "tall" fractures (Figure 8c). These notches show the same shifting behavior as the spectral peaks although the changes in frequency are smaller. These characteristics of the spectra of reflected waves can be used as a diagnostic tool for detecting and characterizing a layer of parallel vertical fractures in the subsurface.

IV. CONCLUSIONS

In this article, we presented an efficient numerical technique for examining the three-dimensional scattering of plane elastic waves by periodic, two-dimensional structures containing fractures. Using this method, we studied the changes in the characteristics of reflection seismograms as a function of incidence angle, wave frequency, and fracture parameters including fracture height, spacing, and stiffness.

For an incident low-frequency P wave, the results of the static effective medium approximation and the explicit simulations by our method were identical. This was somewhat surprising for us because the fractures have a finite height that is relatively small compared to the wavelength, even though the effective medium approximation assumes fractures with an infinite height. For an incident high-frequency wave, the results showed that the scattering from individual fractures and multiple reflections between fractures results in strong reverberations (coda) in seismograms for high-frequency waves. These reverberations indicate the presence of the fractures with spacings similar to the wavelength of the probing waves, and the magnitude of the reverberation is sensitive to both geometry and the stiffness of the fractures. To delineate the contribution of each effect quantitatively, however, further extensive parametric studies should be performed.

Unlike the low-frequency case, the reverberations in the high-frequency seismograms can obscure the azimuthal anisotropy of seismic signatures such as amplitude anisotropy of the scattered *Sh* and *Sv* waves. We demonstrated that for periodic, regular and near-regular fracture spacings, systematic changes can occur in the spectral profiles of high-frequency seismograms as a function of azimuthal angle, which can be an alternative diagnostic tool for identifying the fracture orientations.

Although only limited and simple cases were examined in this article, we emphasize that more realistic, complex geometry and material properties, such as heterogeneous layering, non-planar fractures, non-uniform fracture stiffness, can be modeled by modifying the FEM mesh for the unit cell. Thus, this technique provides computationally inexpensive solutions for studying the fundamental characteristics of elastic waves scattered by aligned fractures without resorting to extensive three-dimensional computations.

ACKNOWLEDGMENTS

This work has been supported by the Assistant Secretary for Fossil Energy, Office of Natural Gas and Petroleum Technology, through the National Energy Technology Laboratory of the U.S. Department of Energy under Contract No. DE-AC03-76SF200098.

REFERENCES

[1] Chang, C.-H. and G.H.F. Gardner, 1997, Effects of vertically aligned subsurface fractures on seismic reflections: A physical model study, *Geophysics*, **62(1)**, 245-252.

[2] Schoenberg, M.A., S. Dean and C.M. Sayers, 1999, Azimuth-dependent tuning of seismic waves reflected from fractured reservoirs, *Geophysics*, **64(4)**, 1160-1171.

[3] Beretta, M.M., G. Bernasconi and G. Drufuca, 2000, Linearized inversion of vertically fractured media, *Geophys. J. Int.*, **143**, 965-968.

[4] Shen, F. and M.N. Toksoz, 2000, Scattering characteristics in heterogeneously fractured reservoirs from waveform estimation, *Geophys. J. Int.*, **140**, 251-266.

[5] Lynn, H.B., K.M. Simon, M. Layman, R. Schneider, C.R., Bates and M. Jones, 1995, Use of anisotropy in P-wave and S-wave data for fracture characterization in a naturally fractured gas reservoir, *The Leading Edge*, **14**, 887-893.

[6] Achenbach, J.D., M. Kitahara, Y. Mikata and D.A. Sotiropoulos, 1988, Reflection and transmission of plane waves by a layer of compact inhomogeneities, *PAGEOPH*, **128**, 101-118.

[7] Hirose, S. and M. Kitahara, 1991, Scattering of elastic waves by a crack with spring-mass contact, *Int. J. Num. Meth. Engng.*, **31**, 789-801.

[8] Liu, E., T. Pointer, J.A. Hudson and J.H. Queen, 1998, Numerical modeling of seismic wave propagation in media with distributed inclusions, Expanded Abstract, 68th SEG Annual Meeting, New Orleans, 1933-1936.

[9] Coates, R.T. and M.A. Schoenberg, 1995, Finite-difference modeling of faults and fractures, *Geophys*., **60**, 1514-1526.

[10] Schoenberg, M.A. and Nihei, K.T., S. Nakagawa and L.R. Myer, 2001, Scattering from reservoirs with discrete fractures, Proc. EAGE/SEG Research Workshop on Reservoir Rocks, Pau.

[11] Hennion, A.C., R. Bossut and J.N. Decarpigny, 1990, Analysis of the scattering of a plane acoustic wave by a periodic elastic structure using the finite element method: Application to compliant tube gratings, *J. Acoust. Soc. Am.*, **87(5)**, 1861-1870.

[12] Hladky-Hennion, A.-C. and J.N. Decarpigny, 1991, Analysis of the scattering of a plane acoustic wave by a doubly periodic structure using the finite element method: Application to Alberich anechoic coatings, *J. Acoust. Soc. Am*, **90(6)**, 3356-3367.

[13] Hughes, T.J.R, 1987, *The Finite Element Method, Linear Static and Dynamic Finite Element Analysis*, Prentice-Hall, Englewood Cliffs, New Jersey.

[14] Henshell, R.D. and K.G. Shaw, 1975, Crack tip finite elements are unnecessary, *Int. J. Num. Methods in Engng.*, **9**, 495-507.

[15] Barsoum, R.S., 1976, On the use of isoparametric finite elements in linear fracture mechanics, *Int. J. Num. Methods in Engng.*, **10,** 25-37.

[16] Schoenberg, M.A., 1980, Elastic wave behavior across linear slip interfaces, *J. Acoust. Soc. Am.*, **68**, 1516-1521.

[17] Baik, J.-M. and R.B. Thompson, 1984, Ultrasonic scattering from imperfect interfaces: A quasi-static model, *J. Nondestuct. Eval.*, **4**, 177-196.

[18] Schoenberg, M.A. and C.M. Sayers, 1995, Seismic anisotropy of fractured rock, *Geophys.* **60**(1), 204-211.

[19] Krenk, S. and H. Schmidt, 1982, Elastic wave scattering by a circular crack, *Phil. Trans R. Soc. Lond. A.*, **308**, 167-198.

Figure 1 Near-parallel vertical fractures in sandstone. Chaco canyon, NM.

Figure 2 A model fractured medium containing periodic fractures. The heterogeneous layer containing fractures (domain Ω_0) is modeled using FEM and the bounding homogeneous halfspaces (Ω_+ and Ω-) are modeled by the plane wave method.

Figure 3 Three-dimensional snapshots of plane waves propagating through a layer containing equally spaced parallel open fractures. The incident wave is a P wave (Ricker wavelet) with a wavelength approximately 1.7 times the fracture spacing.

Figure 4 Source-receiver configuration for the numerical simulations. The locations of the source and the receiver are changed symmetrically around a single vertical axis going through a fracture. For specifying the dip (θ) and azimuthal (ϕ) angles, the point of reflection on the fractured layer is assumed to be located slightly (2 m) above the top ends of the fractures that are 100 m below the source-and-receiver level.

Figure 5 An example of FE mesh used for computing the wave scattering by equally spaced (4-m spacings), 8-m tall fractures. Both mesh refinement and the distorted mesh (quarter-node) techninque were applied to the ends of the fracture.

Figure 6 *z*-, *r*- and *t*-component seismograms computed for the "low-frequency" cases (Figure 6a) and the "high-frequency" cases (Figure 6b). Angles of incidence (θ: dip angle, ϕ: azimuthal angle) are indicated on the right edge of the plots. For the "low-frequency" cases, arrivals of

three wave modes are clearly seen (indicated as *P*, *Sv* and *Sh* below the wavelets for the θ=30° cases). For the "high-frequency' cases, mutiple scattering (coda) dominates the seismograms and *P* and *Sv* waves are difficult to distinguish.

Figure 7a "Low-frequency" waveforms for "soft, short and regular" fractures.

Figure 7b "High-frequency" waveforms for "soft, short and regular" fractures.

Figure 7c "High-frequency" waveforms for "stiff, short and regular" fractures.

Figure 7d "High-frequency" waveforms for "soft, long and regular" fractures.

Figure 7e "High-frequency" waveforms for "soft, short and irregular" fractures.

Figure 7 Azimuthal changes in the *z*-component waveforms of reflected waves for the incidence dip angle of θ=45°. Direct arrivals (Incident waves) are not shown. For comparison, predictions by the static effective medium approximation are shown in dotted lines.

Figure 8a Frequency response for "soft, short and regular" fractures.

Figure 8b Frequency response for "soft, short and regular" fractures.

Figure 8c Frequency response for "stiff, short and regular" fractures.

Figure 8d Frequency response for "soft, long and regular" fractures.

Figure 8e Frequency response for "soft, short and irregular" fractures.

Figure 8 Spectra of waveforms shown in Figure 6b to 6 e normalized by the incident wave spectra. All plots exhibit a trend that shows shifts of spectral peaks (as indicated by solid triangles) and valleys to higher frequencies with increasing azimuthal angle.

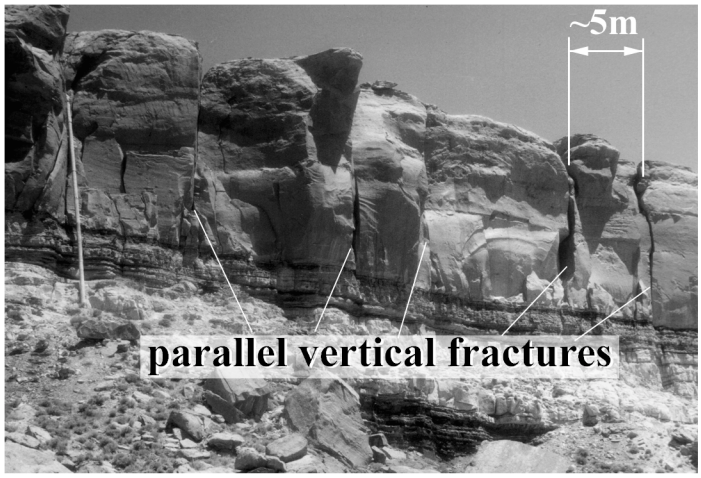

Figure 1

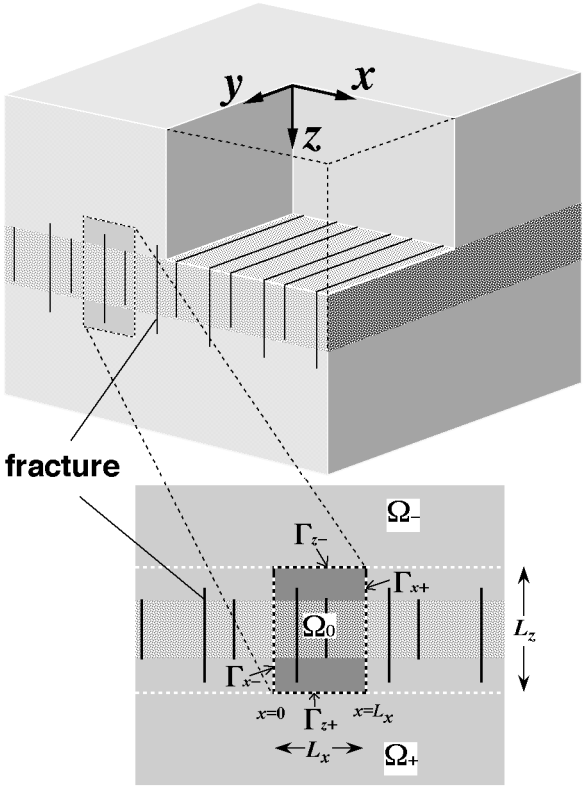

Figure 2

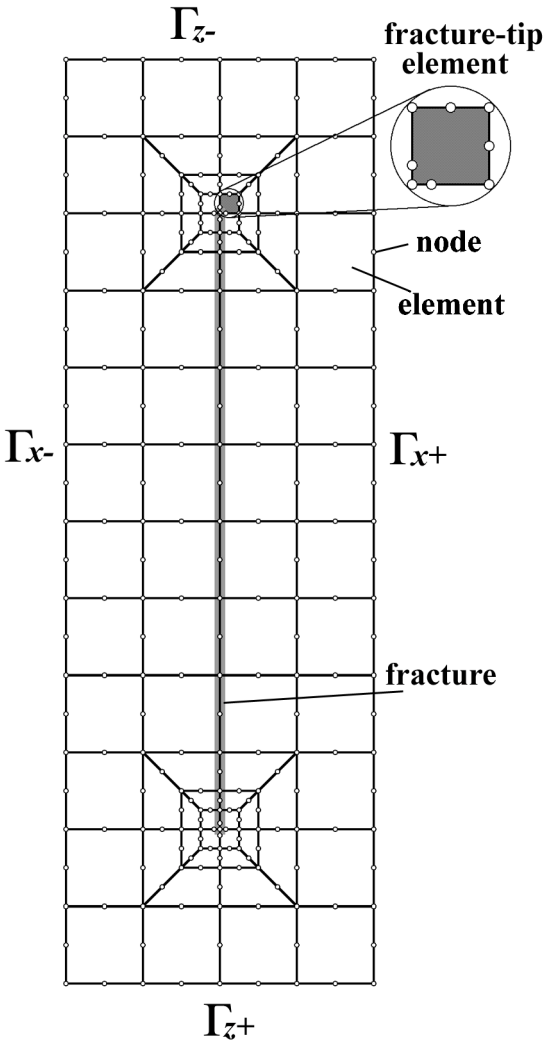

Figure 3

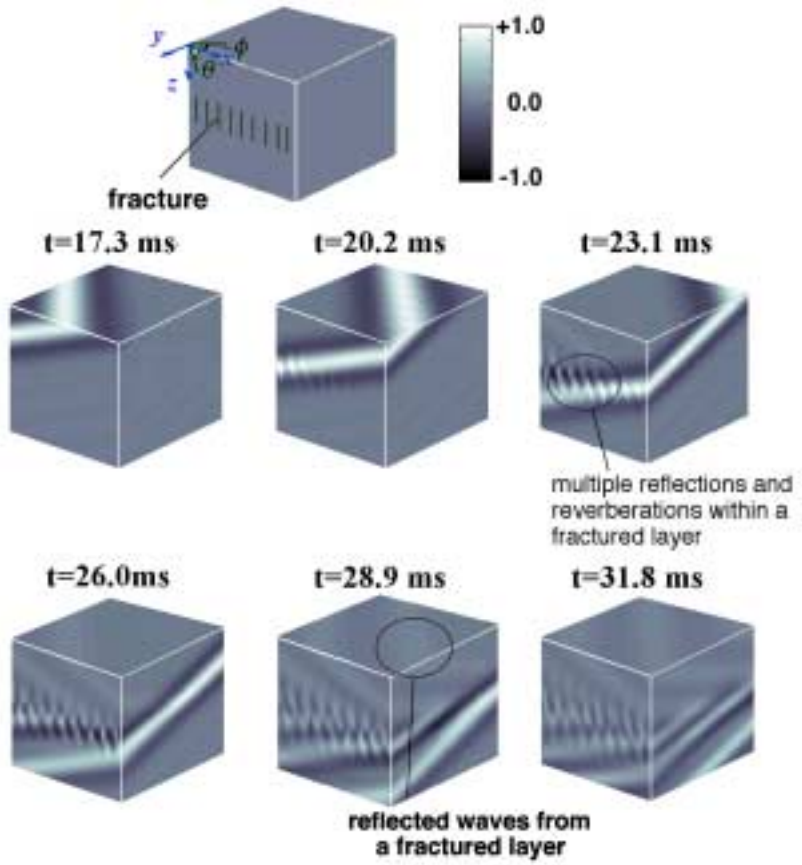

Figure 4

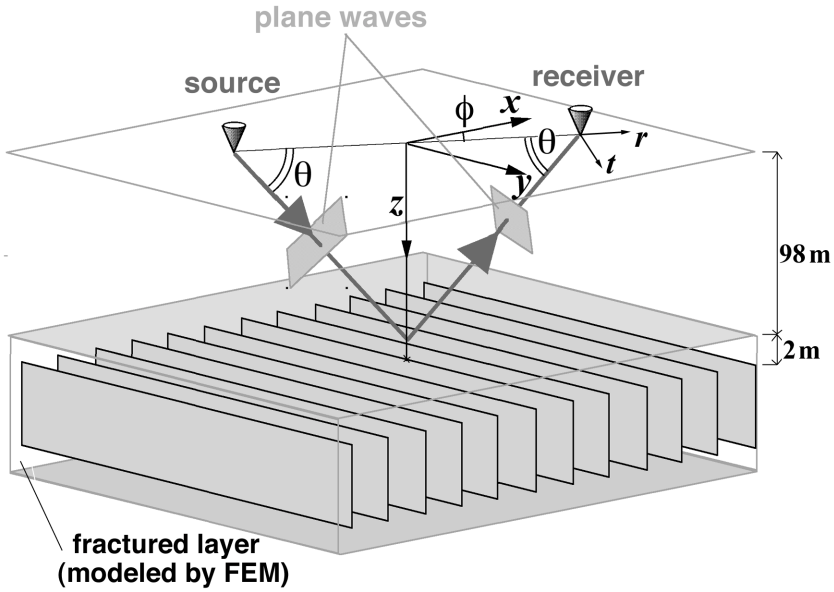

Figure 5

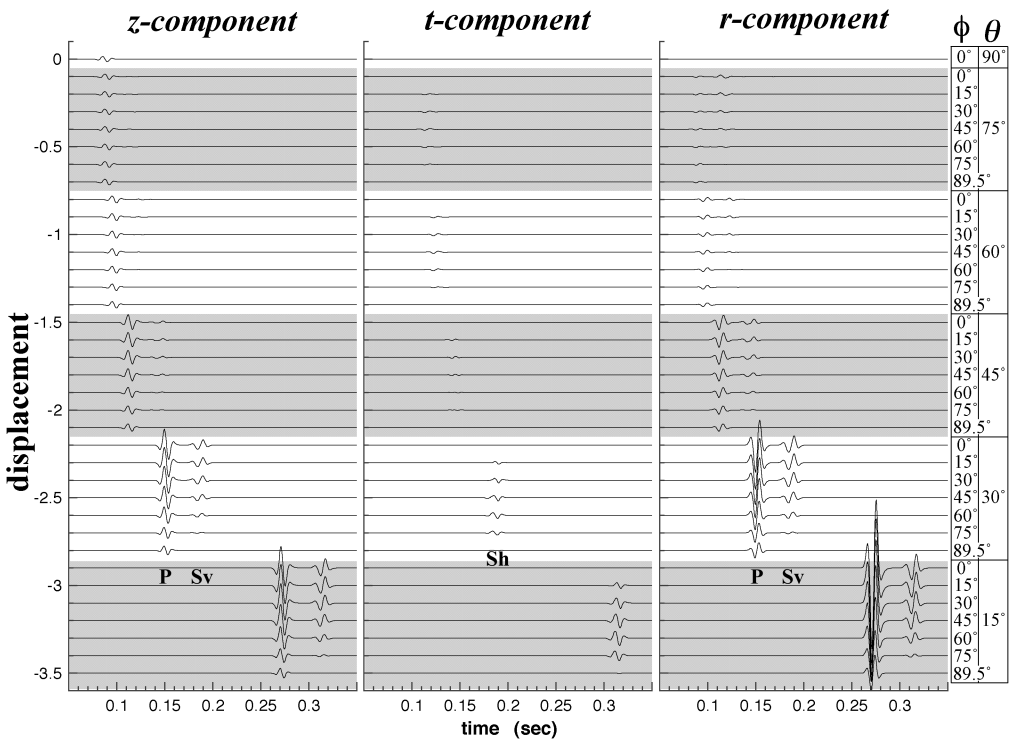

Figure 6a

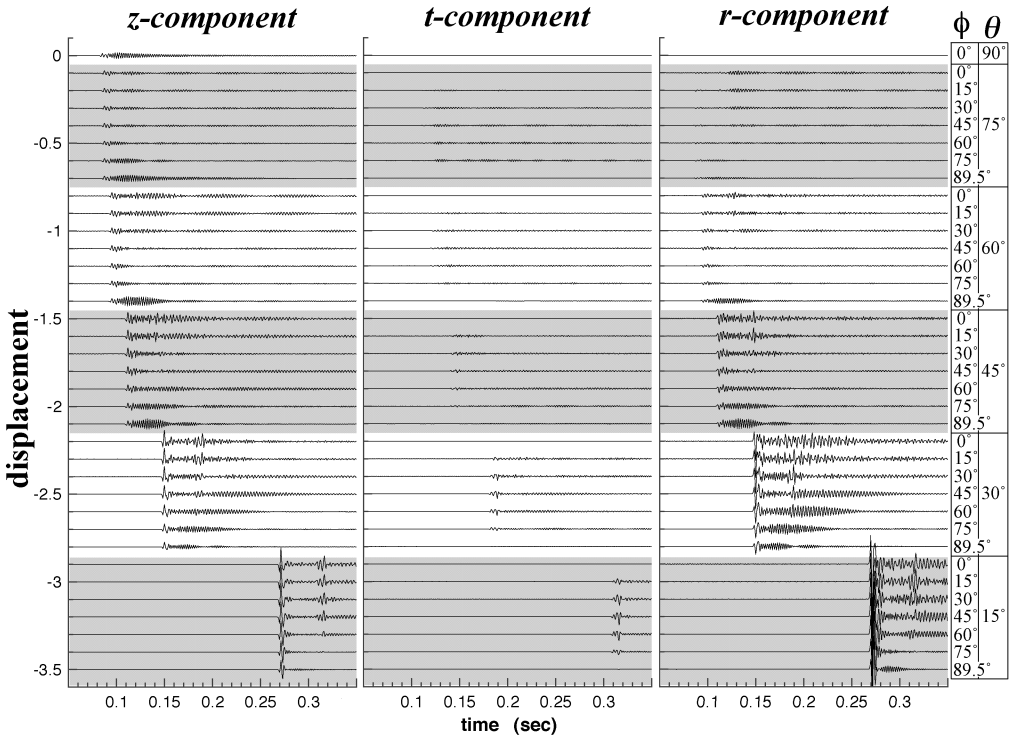

Figure 6b

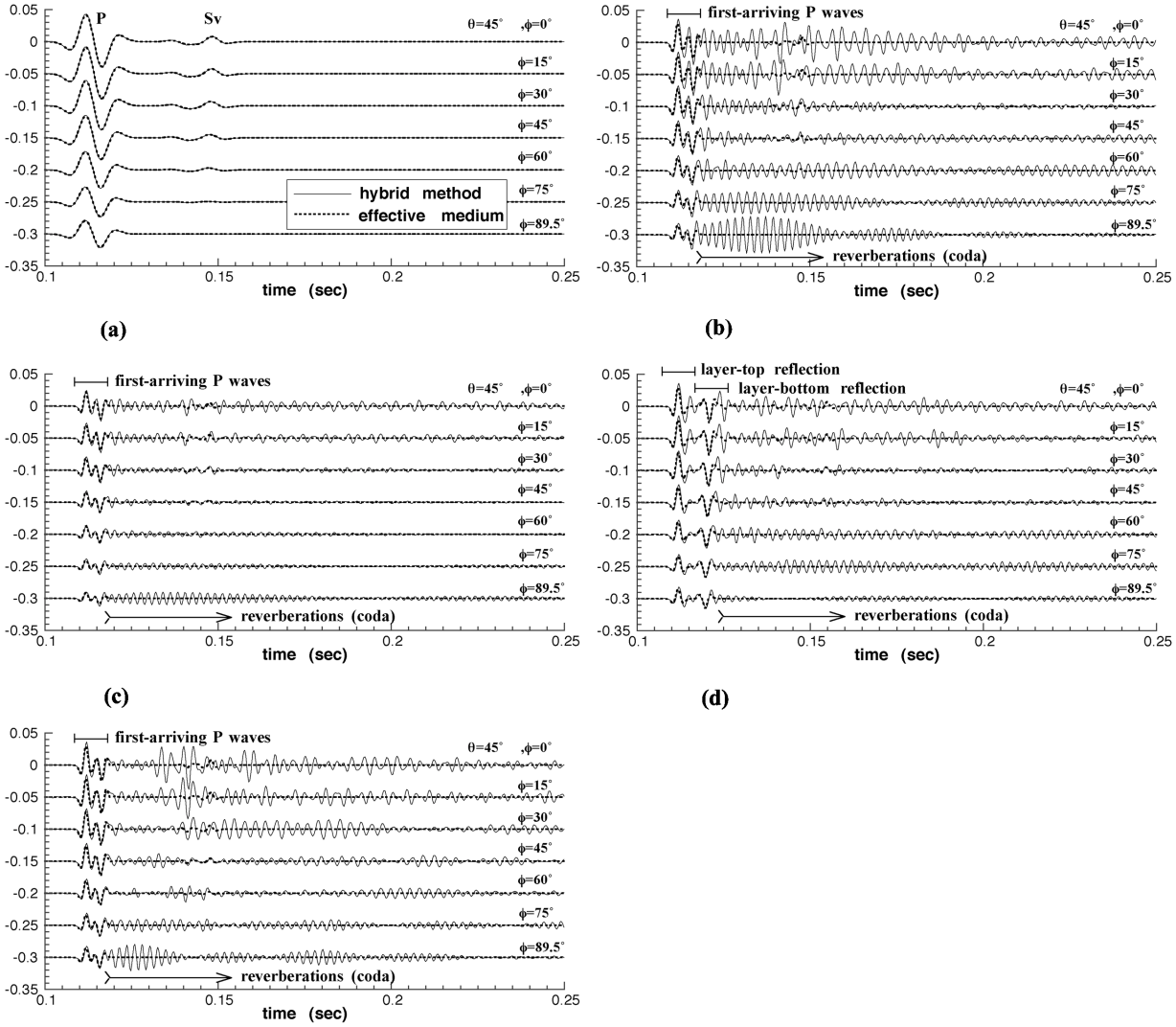
P
Sv
θ=45° ,ϕ=0°
ϕ=15°
ϕ=30°
ϕ=45°
ϕ=60°
ϕ=75°
ϕ=89.5°
hybrid method
effective medium
time (sec)
(a)
first-arriving P waves
reverberations (coda)
(b)
(c)
layer-top reflection
layer-bottom reflection
(d)
(e)

Figure 7

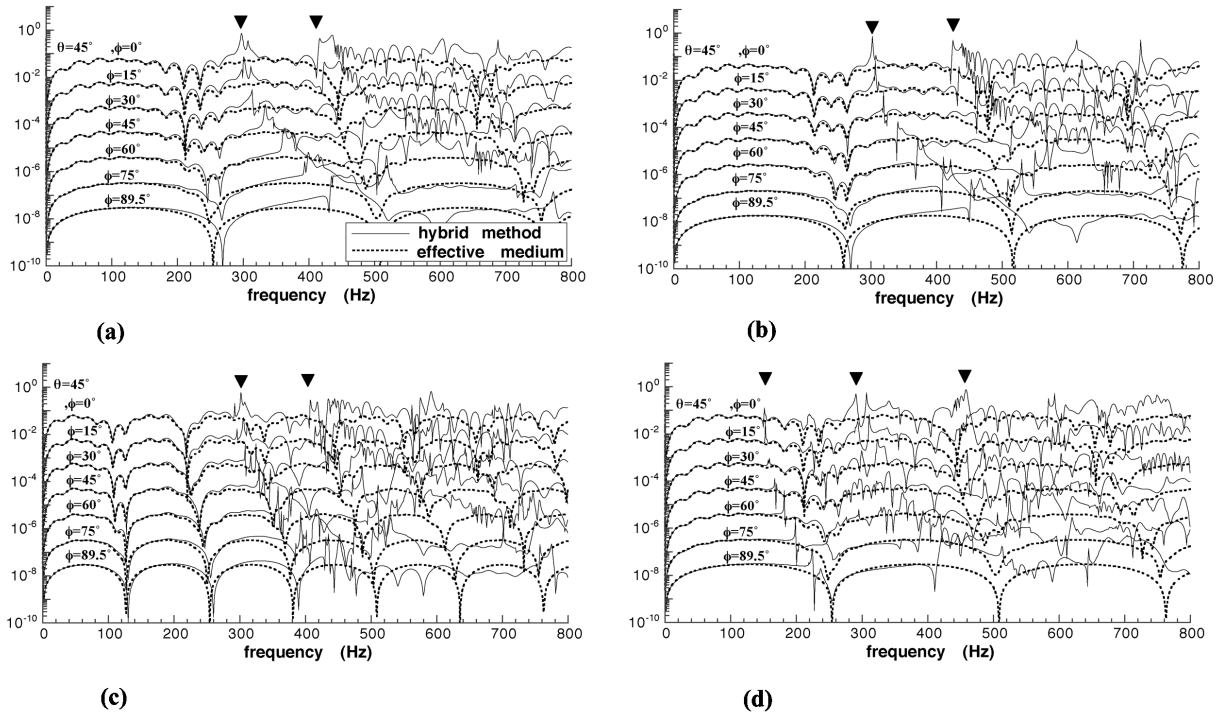
θ=45° ,ϕ=0°
ϕ=15°
ϕ=30°
ϕ=45°
ϕ=60°
ϕ=75°
ϕ=89.5°
hybrid method
effective medium
frequency (Hz)
(a)
(b)
(c)
(d)

Figure 8